Article

In Pursuit of Next Generation N-Heterocyclic Carbene-Stabilized Copper and Silver Precursors for Metalorganic Chemical Vapor Deposition and Atomic Layer Deposition Processes

Ilamparithy Selvakumar [1,†], Nils Boysen [2,†], Marco Bürger [1] and Anjana Devi [1,2,*]

1 Inorganic Materials Chemistry, Ruhr University Bochum, 44801 Bochum, Germany; ilamparithy.selvakumar@ruhr-uni-bochum.de (I.S.); marco.buerger@ruhr-uni-bochum.de (M.B.)
2 Fraunhofer IMS, 47057 Duisburg, Germany; nils.boysen@ims.fraunhofer.de
* Correspondence: anjana.devi@ruhr-uni-bochum.de
† These authors contributed equally to this work.

Abstract: Volatile, reactive, and thermally stable organometallic copper and silver complexes are of significant interest as precursors for the metalorganic chemical vapor deposition (MOCVD) and atomic layer deposition (ALD) of ultra-thin metallic films. Well-established Cu^I and Ag^I precursors are commonly stabilized by halogens, phosphorous, silicon, and oxygen, potentially leading to the incorporation of these elements as impurities in the thin films. These precursors are typically stabilized by a neutral and anionic ligand. Recent advancements were established by the stabilization of these complexes using N-heterocyclic carbenes (NHCs) as neutral ligands. To further enhance the reactivity, in this study the anionic ligand is sequentially changed from β-diketonates to β-ketoiminates and β-diketiminates, yielding two new Cu^I and two new Ag^I NHC-stabilized complexes in the general form of [M(NHC) (R)] (M = Cu, Ag; R = β-ketoiminate, β-diketiminate). The synthesized complexes were comparatively analyzed in solid, dissolved, and gaseous states. Furthermore, the thermal properties were investigated to assess their potential application in MOCVD or ALD. Among the newly synthesized complexes, the β-diketiminate-based [Cu(*t*BuNHC) (NacNacMe)] was identified to be the most suitable candidate as a precursor for Cu thin film deposition. The resulting halogen-, oxygen-, and silicon-free Cu^I and Ag^I precursors for MOCVD and ALD applications are established for the first time and set a new baseline for coinage metal precursors.

Keywords: copper; silver; ALD; MOCVD; N-coordinated precursors

1. Introduction

Copper and silver, two prominent elements among the coinage metals group, possess remarkable properties in their bulk form such as very low electrical resistivity (16.78 $n\Omega^{-1}$ m^{-1} and 15.9 $n\Omega^{-1}$ m^{-1}, respectively) and thermal conductivity (398 W/m K and 429 W/m K, respectively) [1–3]. Especially in the form of thin films, they can be considered as an essential component in various electronic, optoelectronic, and photovoltaic applications [4–7]. Especially for the microelectronic industry, copper interconnects are highly interesting and typically require ultra-thin metallic seed layers before the trenches are completely filled by electrochemical deposition [8,9]. On the other hand, ultra-thin metallic silver films are highly desired for application as transparent electrodes, which are very important building blocks for solar cells and optoelectronics [10–12]. Continuous and ultra-thin films of silver reaching a critical thickness of below 10 nm that are conductive and at the same time transparent are crucial for such applications [13–18]. Both materials can be deposited in an ultra-thin fashion by vapor-phase deposition techniques such as physical vapor deposition (PVD), chemical vapor deposition (CVD), or atomic layer deposition (ALD) [19,20].

However, the deposition of thin films via PVD follows a line-of-sight (LOS) mechanism, leading to a non-conformal coating of substrates among its other shortcomings, such as the complicated scalability of the processes. Such deposited films lead to non-homogenous thickness on substrates with intricate shapes undesired for their respective applications [21,22]. On the contrary, CVD and ALD primarily follow a non-LOS approach for the growth of the film that usually leads to processes with higher conformality, which is especially true for ALD [19,23]. In both cases, a metalorganic precursor is typically employed for the deposition of various material systems. While the precursors should be highly volatile and reactive for ALD, in the case of CVD, the precursor molecule should ideally decompose on the substrate, while ALD evidently relies on the self-limiting surface reactions of the precursors, and thus precursor stability is one of the prerequisites. The volatility, reactivity, and thermal stability of a precursor can be effectively engineered by introducing an organic ligand in the coordination sphere of the metal that results in distinct changes in the physico-chemical properties of the precursors.

Metalorganic Cu[I] and Ag[I] complexes have remarkably similar bonding and physio-chemical properties [24]. Copper complexes can be usually found in oxidation states of +I and +II, while stable silver complexes are mostly limited to the oxidation states of +I. For MOCVD and ALD, a vast number of Cu[I], Cu[II], and Ag[I] precursors are known. For the sake of comparability and scope of our study, we are only discussing Cu[I] and Ag[I] complexes in the following section. A comprehensive review on available copper (I and II) and silver (I) precursors is reported by Hagen et al. [25]. The current challenge for Cu[I] precursors is to find well-performing precursors that are free of halogens, oxygen, phosphorous, or silicon, owing to their tendency to either contaminate the deposited films or poison the surface of the substrate. Moreover, current heteroleptic Cu[I] precursors like [Cu(TMVS) (hfac)] (TMVS = trimethylvinylsilyl, hfac = hexafluoroacetylacetone) (Figure 1 (inset A)) are stabilized by neutral alkene, which is unstable and has been reported to disproportionate upon vaporizing at higher temperatures, leading to low saturation of the precursor over the substrate and the potential incorporation of fluorine [26]. The all-nitrogen-coordinated homoleptic Cu-amidinate dimer has been reported to show very good reactivity and high thermal stability, such that it is currently a well-established precursor for ALD and CVD of Cu and CuO films. This also highlights the increase in reactivity upon introducing N-coordinating ligands. However, the option to further functionalize the ligand sphere is limited, which would be beneficial for having selective deposition processes and surface reactions [27,28].

One strategy to obtain mononuclear complexes is to employ neutral coordinating ligands. A natural way of enhancing the stability between the neutral ligand and the metal ion is to apply carbenes as neutral ligands. These ligands are very well established and mature in the field of catalysis; however, potential precursors for copper, stabilized by carbenes for ALD, were first reported by Coyle et al. in the year of 2013 (Figure 1 (inset C)) [29]. The neutral N-heterocyclic carbene (NHC) ligand together with the anionic hexamethyl-disilazide (HMDS) ligand resulted in a volatile, reactive, and at the same time thermally stable complex that could be used for copper ALD at a deposition temperature of 225 °C. The purity of the resulting copper film deposited via PE-ALD (plasma-enhanced ALD) using [Cu(*i*PrNHC) (HMDS)] has not been exactly determined in this study. Nevertheless, carbene-stabilized copper precursors have revealed significantly improved physico-chemical properties compared to the established Cu[I] precursors at this time [29]. A very similar precursor with a tert-butyl NHC ligand, namely, [Cu(*t*BuNHC) (HMDS)], has been used for atmospheric pressure plasma-enhanced spatial ALD (APP-ALD) of copper thin films at a very low temperature of 100 °C for the first time. Impurity levels were under the detectable limits of X-ray photoelectron spectroscopy (XPS), and saturation of the precursor on the surface could be retained [30].

The available Ag[I] precursors for MOCVD and ALD are very limited in comparison to copper precursors. The well-established silver precursors for MOCVD and ALD among others include the [Ag(C$_2$F$_5$COO)]$_2$ and [Ag(PEt$_3$) (fod)] (fod = 6,6,7,7,8,8,8-heptafluoro-

2,2-dimethyl-3,5-octanedionate). Both the precursors are strongly stabilized by fluorine backbones for enhanced volatility, which can lead to film impurities [31,32]. To date, there has not been significant progress towards developing a halogen-, oxygen-phosphorous-, and silicon-free silver precursor for MOCVD and ALD. As mentioned earlier, similar NHC ligands can also be applied to silver, which significantly stabilizes the reactive complexes. As an example, [Ag(*t*BuNHC) (HMDS)] showed promising physico-chemical characteristics for ALD. Subsequent deposition experiments yielded pure metallic silver films via APP-ALD for solar cell applications at a record low deposition temperature of only 60 °C [33,34].
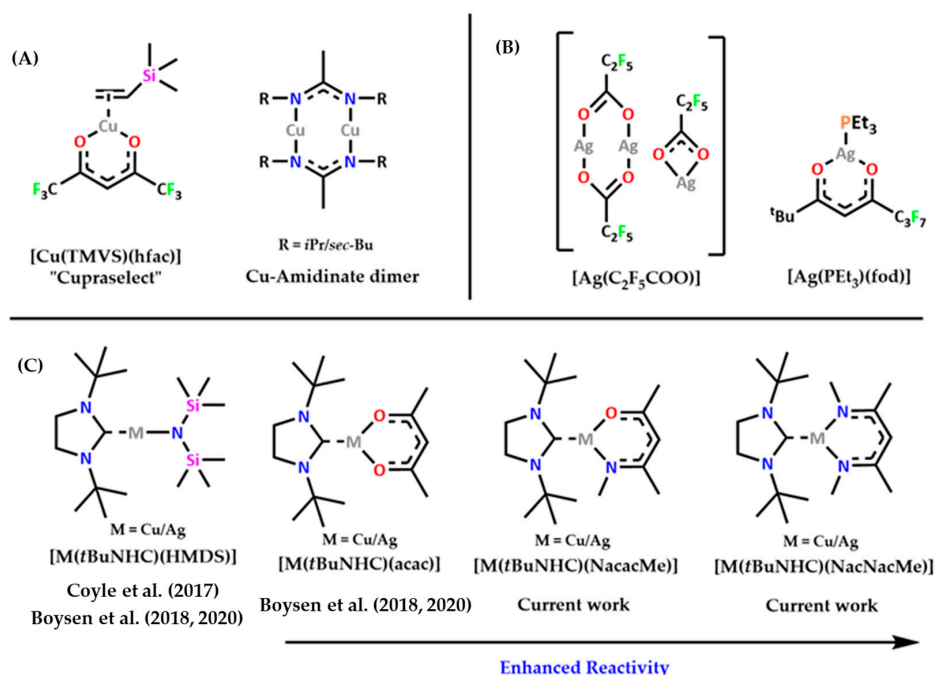
Figure 1. Selected examples for known copper (I) precursors and silver (I) precursors for the CVD and ALD of metallic thin films; (**A**) commercially known "cupraselect" and binuclear copper amidinate. (**B**) Established silver (I) precursors for the CVD and ALD of metallic thin films. (**C**) Established NHC-based copper and silver complexes with their evolution to new complexes by replacing the anionic HMDS ligands with NacacMe and NacNacMe.

To investigate the influence of the anionic backbone in such NHC-stabilized complexes, further functionalization was carried out by Boysen et al., reporting a row of differently functionalized [M(*t*BuNHC) (dktacac)] (dkt = β-diketonate; M = Cu, Ag) complexes (*t*BuNHC = tertiarybutyl-N-Heterocyclic carbene, acac = acetylacetone) along with the proof of deposition of copper via thermal ALD at moderate temperatures of 145–160 °C and with hydroquinone as the co-reactant [35]. The resulting nanoparticulate films contained residual oxygen and carbon impurities that might be caused by the precursor and co-reactant at the same time. The silver complexes evaluated in this study only provided poor thermal stability and were thus not applicable for ALD experiments. Thus, the library of silver precursors for ALD is staggeringly low, and new heteroleptic precursors need to be developed. Additionally, the number of available copper and silver precursors that only feature carbon and nitrogen atoms in the ligand sphere is very low.

Our group has frequently reported enhanced reactivity by the introduction of different nitrogen coordinated (amidinates, guanidinates, diazadienyls, etc.) metal complexes, which has also led to the elimination of possible halogen and oxygen impurities [36–38]. To expand the library of NHC-based copper and silver precursors, 1,3-ketiminates (Nacac) and 1,3-diketimines (NacNacs) as anionic ligands are employed in this work. Thus, halogen-free, phosphine-free, oxygen-free, and silyl-free precursors on the basis of the NacNac ligand class are established for Cu^I and Ag^I complexes as potential precursors for MOCVD and ALD. The reactivity profile of the complexes can be precisely tuned by including O,O-

coordination in diketonates, N,O-coordination in ketiminates, and N,N-coordination in diketimines. Thus, a new generation of highly reactive precursors without heteroatoms other than C and N in the ligand sphere is developed in this study and consequently evaluated for their potential use in MOCVD and ALD processes for the formation of metallic thin films.

2. Materials and Methods

2.1. General Experimental

All synthesized complexes and starting materials were either air sensitive or moisture sensitive or both. The reaction procedures were carried out with various sophisticated Schlenk techniques under argon (Air Liquide, 99.99%, Düsseldorf, Germany) as the inert atmosphere. The flasks and glassware were used upon being oven-dried and further baked under vacuum before usage. The synthesized starting materials [Cu(*t*BuNHC) (HMDS)] and [Ag(*t*BuNHC) (HMDS)] were stored in an argon-filled glove box (Mbraun, Munich, Germany). Commercially available chemicals were used without any further purification. Solvents used were dried using an SPS (solvent purification system) from Mbraun (Munich, Germany) and stored over 4 Å molecular sieves. The NMR solvents used benzene-d_6 and $CDCl_3$ and were degassed and stored over 4 Å molecular sieves inside a glove box. All the NMRs were recorded in Bruker Advance DPX-300 and Bruker Avance III HD AVI400 (Karlsruhe, Germany) with TMS (tetramethylsilane) as the internal standard. Further evaluation of NMR data and structure were completed using Mestrenova version 14 and Mercury 3.0 versions, respectively. The pKa values for the anionic ligands were obtained from Scifinder and calculated using the Advanced Chemistry Development (ACD/Labs) Software V11.02. Silver compounds were either handled in brown glassware or glassware wrapped with aluminum foil to protect them from exposure to light. Details on the analysis of the complexes by liquid-injection field desorption ionization mass spectrometry (LIFDI-MS) can be found in the supporting information. In general, the analysis was achieved with either a Jeol AccuTOF GCv (Freising, Germany) spectrometer or an Orbitrap in an Exploris 120 instrument from ThermoFisher Scientific, Bremen, Germany. Both devices were equipped with a LIFDI source from Linden CMS, Weyhe, Germany. The single crystal structures were recorded using Oxford Rigaku Diffraction Synergy S (Neu-Isenburg, Germany) with copper as the X-ray source. Single crystals of the respective Cu and Ag compounds were crystallized from concentrated solutions in hexane, pentane, THF, or diethyl ether. A suitable crystal was selected under a microscope in perfluoroether oil and mounted inside a flexible loop on the diffractometer. The crystals were cooled to 100 K during data collection. Using Olex2, the structure was solved with the SHELXT structure solution program using Intrinsic Phasing and refined with the SHELXL refinement package using least squares minimization. IR measurements were performed on an FTIR spectrometer, Spectrum Two by PerkinElmer (Rodgau, Germany), utilizing a UATR Two ATR-unit by PerkinElmer, placed in an argon-filled glove box. Thermogravimetric analysis (TGA) and differential scanning calorimetry (DSC) were performed on a Netzsch STA 409 PC (Selb, Germany) at ambient pressure (sample size $\approx$ 10 mg), with a heating rate of 5 °C min-1 (N_2 flow rate = 300 mL min^{-1}), placed in an argon (Air Liquide, 99.995%) filled glove box (SylaTech, Walzbachtal, Germany).

2.2. Preparation of Anionic Ligands

2.2.1. 4-(Methylamino)pent-3-en-2-one (NacacMe)

The synthesis is based on a modified version of the literature reports [39,40]. In an oven-dried 100 mL Schlenk flask, 20.5 mL/20 g of pent-3-en-2-one (200 mmol, 1 eq.) was dissolved in 40 mL of toluene. A total of 17.3 mL/15.51 g of 40% aqueous methyl amine (200 mmol, 1 eq.) solution was added dropwise, while the reaction mixture was stirred. The reaction mixture was refluxed at 115 °C overnight. Upon completion, the reaction mixture was cooled down and concentrated to $\frac{1}{4}$th of its volume and stored at -30 °C. The colorless crystals were filtered and dried, yielding colorless crystalline solid (17 g, 150 mmol, yield: 75%). The ^{1}H NMR shifts match the values known in the literature.

^{1}H NMR (400 MHz, C$_6$D$_6$) δ = 10.97 (s, CH$_3$–N*H*–), 4.89 (s, –C–C*H*–C–), 2.04 (d, C*H$_3$*–NH–), 1.25 (s, C*H$_3$*).

2.2.2. N-Methyl-4-(methylimino)pent-2-en-2-Amine (NacNacMe)

The synthesis of NacNacMe is based on a modified version of the literature reports using Meerwein's salt [41,42]. A total of 8 g of triethyl tetrafluroborate salt (44.19 mmol, 1 eq.) was dissolved in 15 mL of DCM (dichloromethane) in a Schlenk flask. In another Schlenk flask, 5 g of 4-(methylamino)pent-3-en-2-one (44.19 mmol, 1 eq.) was dissolved in 30 mL of DCM. The salt solution was then transferred to the NacacMe solution and then allowed to stand still for 30 min. With vigorous stirring, methyl amine (5.5 mL, 33 wt% in ethanol, 44 mmol, 1 eq.) was added dropwise to the reaction mixture. The reaction mixture was further filtered to remove excess borate salt. The bright yellow solution was concentrated and stored at −30 °C to yield colorless tetraborate salt of NacNacMe. The crystals were filtered and cracked using 50 mL of 0.5 M NaOMe in methanol. The volatiles were removed, and the white solid residue was extracted in toluene, which upon concentration of the solvent, yielded white color microcrystalline solid (1 g, 8 mmol, yield: 18%). The ^{1}H NMR shifts match the values known in the literature.

^{1}H NMR (400 MHz, C$_6$D$_6$) δ [ppm] = 11.14 (s, CH$_3$–N*H*–), 4.63 (s, C*H$_3$*), 2.79 (s, C*H$_3$*–NH–), 1.66 (s, C*H$_3$*).

2.3. Preparation of Starting Material Complexes

The *t*BuNHC (tertiary butyl N-Heterocyclic carbene) chloride salt was synthesized based on the literature reports with minimal modifications [35,43]. The complexes were synthesized utilizing a one-pot synthesis route published by Boysen et al. [30].

2.3.1. [Cu(tBuNHC) (HMDS)]

A total of 2.7 g of copper chloride (27.27 mmol, 1 eq.), 5.97 g of *t*BuNHC-chloride (27.27 mmol, 1 eq.), and 13.17 g of Li(HMDS) were taken in a 200 mL Schlenk flask. A total of 80 mL of THF as the solvent was added while stirring. The reaction mixture was refluxed at 75 °C. Upon reaction completion, the solvent was removed, and the crude grey product was extracted in n-hexane. The extracted colorless solution was concentrated to $\frac{1}{4}$th of the volume and stored at −30 °C. The colorless crystals were filtered with a cannula filtration and dried to give white crystals (7.75 g, 19 mmol, yield: 70%). The ^{1}H NMR shifts match the values known in the literature.

^{1}H NMR (400 MHz, C$_6$D$_6$) δ [ppm] = 2.58 (s, –C*H$_2$*–C*H$_2$*–), 1.33 (s, (C*H$_3$*)C), 0.57 (s, (C*H$_3$*)$_3$–Si).

2.3.2. [Ag(tBuNHC) (HMDS)]

A total of 3.5 g of silver chloride (24.42 mmol, 1 eq.), 5.34 g of *t*BuNHC-chloride (24.42 mmol, 1 eq.), and 11.79 g of Li(HMDS) (24.42 mmol, 2 eq.) were taken in a 200 mL Schlenk flask. A total of 80 mL of tetrahydrofuran (THF) as the solvent was added. The reaction mixture was refluxed at 75 °C. Upon reaction completion, the solvent was removed, and the crude grey product was extracted using 50 mL n-hexane three times. The extracted colorless solution was concentrated to $\frac{1}{4}$th of the volume and stored at −30 °C. The colorless crystals were filtered and dried to give white crystals. (4.5 g, 10 mmol, yield: 41%). The ^{1}H NMR shifts match the values known in the literature.

^{1}H NMR (400 MHz, C$_6$D$_6$) δ [ppm] = 2.56 (s, –C*H$_2$*–C*H$_2$*–), 1.25 (s, (C*H$_3$*)C), 0.60 (s, (C*H$_3$*)$_3$–Si).

2.4. Preparation of Precursor Complexes

2.4.1. [Cu(tBuNHC) (NacacMe)] (1)

To a 25 mL Schlenk flask, 0.5 g of the starting material, [Cu(*t*BuNHC) (HMDS)] (1.23 mmol, 1 eq.), and 0.14 g of NacacMe (1.23 mmol, 1 eq.) were added. About 10 mL of n-hexane was added to the reaction mixture and stirred for 3 h. Upon reaction completion,

about 1.5 mL of THF was added to dissolve the precipitate, and the homogenous green solution was stored at −30 °C. Colorless crystals were obtained, which were filtered and dried under vacuum, yielding light yellow crystals (0.325 g, 0.94 mmol, yield: 76%).

^{1}H NMR (400 MHz, C_6D_6) δ [ppm] = 5.06 (s, –C–C*H*–C–), 3.34 (s, C*H$_3$*–N–), 2.79 (s, –C*H$_2$*–C*H$_2$*–), 2.25 (s, C–C*H$_3$*), 1.78 (s, C–C*H$_3$*), 1.45 (s, (C*H$_3$*)$_3$C).

^{13}C NMR (75 MHz, C_6D_6) δ [ppm] = 204.3 (C*–Cu), 180.88 (*C*=O), 168.51 (CH$_3$–N), 95.87 ((CH$_3$)$_3$*C*–N), 54.40 (*C*H), 44.90 (*C*H$_2$–*C*H$_2$), 42.54 (*C*–N), 29.72 (*C*H$_3$), 28.45 ((*C*H$_3$)$_3$C), 20.92(*C*H$_3$).

FTIR: v (cm^{-1}) = 2900 cm^{-1} (CH), 1550 cm^{-1} (C=C), 1200 cm^{-1} (C–O).

LIFDI-MS (m/z) = [M-H]: 357.1; experimental: 357.1

2.4.2. [Ag(tBuNHC) (NacacMe)] (2)

To a 25 mL Schlenk flask, 0.5 g of the starting material, [Ag(*t*BuNHC) (HMDS)] (1.11 mmol, 1 eq.), and 0.14 g of NacacMe (1.11 mmol, 1 eq.) were added. About 10 mL of n-hexane was added to the reaction mixture and stirred for 3 h. Upon reaction completion, about 2.5 mL of THF was added dropwise to dissolve the precipitate. Further, the clear dark solution was stored at −30 °C. Colorless crystals were formed, which were filtered and dried for 1 h under vacuum, yielding grey-colored crystals (0.4 g, 0.73 mmol, yield: 66%).

^{1}H NMR (200 MHz, C_6D_6) δ [ppm] = 5.40 (s, –C–C*H*–C–), 5.04 (s, –C–C*H*–C–), 3.44 (s, C*H$_3$*–N–), 3.28 (s, C*H$_3$*–N–), 3.15 (s, –C*H$_2$*–C*H$_2$*–), 2.74 (s, C–C*H$_3$*) 2.51 (s, C–C*H$_3$*) 2.33 (s, C–C*H$_3$*), 1.89 (s, C–C*H$_3$*), 1.29 (s, (C*H$_3$*)$_3$C).

^{13}C NMR (101 MHz, CDCl3) δ [ppm] = 194.84 (*C*=O), 163.91 (CH$_3$–N), 153.68 (*C*H–N), 140.33 ((CH$_3$)$_3$*C*–N), 95.11 (*C*H), 77.36 (*C*H), 57.24 (*C*–N), 45.36 (*C*H$_2$–*C*H$_2$), 31.03 (*C*H$_3$), 29.64 (*C*H$_3$), 29.39 (*C*H$_3$), 29.10 ((*C*H$_3$)$_3$C), 18.73 (*C*H$_3$), C*–Cu not observed.

FTIR: v (cm^{-1}) = 2900 cm^{-1} (CH), 1550 cm^{-1} (C=C), 1200 cm^{-1} (C–O).

2.4.3. [Cu(tBuNHC) (NacNacMe)] (3)

To a 25 mL oven-dried Schlenk flask, 0.5 g of the starting material, [Cu(*t*BuNHC-) (HMDS)] (1.23 mmol, 1 eq.), and 0.15 g of NacNacMe (1.23 mmol, 1 eq.) were added. To this, 10 mL of n-hexane was added, and the reaction mixture was stirred for about 3 h. Upon reaction completion, about 2 mL of THF was added dropwise to dissolve the precipitate. Further, the homogenous purple solution was stored at −30 °C in a freezer for 18 h. Colorless crystals could be seen, which were filtered using a cannula and dried for 1 h under vacuum, yielding purple color cubicle crystals (0.260 g, 0.7 mmol, yield: 57%).

^{1}H NMR (400 MHz, C_6D_6) δ [ppm] = 4.78 (s, –C–C*H*–C), 3.48 (s, C*H$_3$*–N–), 2.81 (s, –C*H$_2$*–C*H$_2$*–), 2.03 (s, –C*H$_3$*), 1.47 (s, (C*H$_3$*)$_3$C).

^{13}C NMR (101 MHz, C_6D_6) δ [ppm] = 205.04 (C*–Cu), 163.98 ((CH$_3$–N)), 94.46 (((CH$_3$)$_3$*C*–N), 54.64 (*C*H), 45.16 ((CH$_3$)$_3$*C*)), 43.28 (*C*–N), 29.62 ((*C*H$_3$)$_3$C)), 21.71(*C*H$_3$).

FTIR: v (cm^{-1}) = 2900 cm^{-1} (CH), 1550 cm^{-1} (C=C), 1200 cm^{-1} (C–O).

LIFDI-MS (m/z) = [M-H]: 370.2; experimental: 370.14.

2.4.4. [Ag(tBuNHC) (NacNacMe)] (4)

In a 25 mL oven-dried Schlenk flask, 0.5 g of the starting material, [Ag(*t*BuNHC-) (HMDS)] (1.11 mmol, 1 eq.), and 0.14 g of NacNacMe (1.11 mmol, 1 eq.) were added followed by 10 mL of n-hexane. The reaction mixture was stirred for a minimum of 3 h. Upon reaction completion, about 2.5 mL of THF was added dropwise to dissolve the precipitate. Further, the clear dark solution was stored at −30 °C. Colorless crystals could be seen, which were filtered and dried, yielding grey-colored crystals (0.205 g, 0.5 mmol, yield: 45%).

^{1}H NMR (400 MHz, C_6D_6) δ [ppm] = 4.67 (s, –C–C*H*–C), 3.61 (s, C*H$_3$*–N–), 2.75 (s, –C*H$_2$*–C*H$_2$*–), 2.11 (s, –C*H$_3$*), 1.36 (s, (C*H$_3$*)$_3$–C).

^{13}C NMR (101 MHz, C_6D_6) δ [ppm] = 213.04 (C*–Cu), 165.61 (((CH$_3$–N)), 92.56 ((CH$_3$)$_3$*C*–N), 54.57 (*C*H), 45.28 ((CH$_3$)$_3$*C*)), 45.21 (*C*H$_2$), 43.50 (*C*–N), 29.86 ((*C*H$_3$)$_3$C), 21.95 (*C*H$_3$).

FTIR: v (cm^{-1}) = 2900 cm^{-1} (CH), 1550 cm^{-1} (C=C), 1200 cm^{-1} (C–O).

LIFDI-MS (orbitrap) (m/z) = [M-H]: 414.19072; experimental: 414.1909.

3. Results and Discussion

3.1. Synthesis of Metal Complexes

Unlike the frequently reported salt metathesis reactions employed for the synthesis of a wide range of MOCVD and ALD precursors [44,45], in this case, we opted for a displacement reaction of the anionic ligand itself as seen in Scheme 1, a modified procedure previously reported by Boyson et al. for [Cu(*t*BuNHC) (acac)] [35]. With a 1:1 ratio of the starting material to that of the ligands NacacMe/NacNacMe, this route was primarily chosen due to the higher basicity of HMDS (pka: 14.40) relative to that of both NacacMe (pka: 6.39) and NacNacMe (pka: 12.95), which is the driving force for the exchange of HMDS. HMDS can be removed conveniently either by reduced pressure or by crystallization of the target complex. All the complexes were crystallized in a solvent mixture of hexane:THF in varying ratios at −30 °C as shown in Table 1. The yields of the product varied significantly for copper and silver analogs. Accordingly, the synthesis of copper complexes resulted in higher yields (>50%) in comparison to the silver analogs. This can be possibly explained by the poor solubility of the silver complexes in non-polar organic solvents like hexane, pentane, and heptane. Conversely, the same silver complexes were highly soluble in THF; thus, the formation of crystals is constrained, resulting in lower yields relative to their copper analogs. The obtained crystals were subjected to SC-XRD (single crystal X-ray diffraction) and FT-IR (Fourier transform infrared) spectroscopy in the solid state along with the NMR characterization in the dissolved state, which is discussed in detail below.

Table 1. Crystallographic and refinement details for compounds herein.

|	**[Cu(*t*BuNHC) (NacacMe)]**	**[Ag(*t*BuNHC) (NacacMe)]**	**[Cu(*t*BuNHC) (NacNacMe)]**
CCDC code	2279240	2279241	2279242
Empirical formula	$C_{17}H_{32}CuN_3O$	$C_{17}H_{32}AgN_3O$	$C_{18}H_{35}CuN_4$
Formula weight	357.99	402.32	371.04
Temperature/K	109.99 (14)	100.2 (4)	109.9 (6)
Crystal system	monoclinic	monoclinic	orthorhombic
Space group	P2$_1$/n	I2/a	Pbca
a/Å	14.4287 (4)	23.29733 (10)	11.16780 (10)
b/Å	14.2916 (2)	16.04937 (8)	11.70100 (10)
c/Å	19.2653 (5)	41.1905 (2)	29.6636 (2)
α/°	90	90	90
β/°	109.120 (3)	97.4656 (4)	90
γ/°	90	90	90
Volume/Å^3	3753.53 (16)	15,270.88 (12)	3876.27 (5)
Z	8	32	8
ρ_{calc}g/cm^3	1.267	1.400	1.272
μ/mm^{-1}	1.671	8.502	1.610
F(000)	1536.0	6720.0	1600.0
Crystal size/mm^3	0.279 × 0.197 × 0.165	0.183 × 0.141 × 0.087	0.269 × 0.177 × 0.087
Radiation	Cu Kα (λ = 1.54184)	Cu Kα (λ = 1.54184)	Cu Kα (λ = 1.54184)
2Θ range for data collection/°	6.708 to 146.116	5.916 to 155.772	5.958 to 153.434
Index ranges	−17 ≤ h ≤ 16, −17 ≤ k ≤ 11, −20 ≤ l ≤ 23	−29 ≤ h ≤ 29, −19 ≤ k ≤ 20, −52 ≤ l ≤ 49	−14 ≤ h ≤ 13, −14 ≤ k ≤ 14, −28 ≤ l ≤ 36
Reflections collected	14,117	97,805	34,158
Independent reflections	7242 [R$_{int}$ = 0.0447, R$_{sigma}$ = 0.0588]	16,028 [R$_{int}$ = 0.0336, R$_{sigma}$ = 0.0190]	3937 [R$_{int}$ = 0.0405, R$_{sigma}$ = 0.0202]
Data/restraints/parameters	7242/0/415	16028/116/861	3937/0/218
Goodness-of-fit on F^2	1.069	1.067	1.045
Final R indexes [I ≥ 2σ (I)]	R$_1$ = 0.0539, wR$_2$ = 0.1440	R$_1$ = 0.0304, wR$_2$ = 0.0805	R$_1$ = 0.0329, wR$_2$ = 0.0945
Final R indexes [all data]	R$_1$ = 0.0708, wR$_2$ = 0.1517	R$_1$ = 0.0328, wR$_2$ = 0.0822	R$_1$ = 0.0356, wR$_2$ = 0.0970
Largest diff. peak/hole/e Å^{-3}	0.44/−0.68	0.70/−0.83	0.47/−0.40
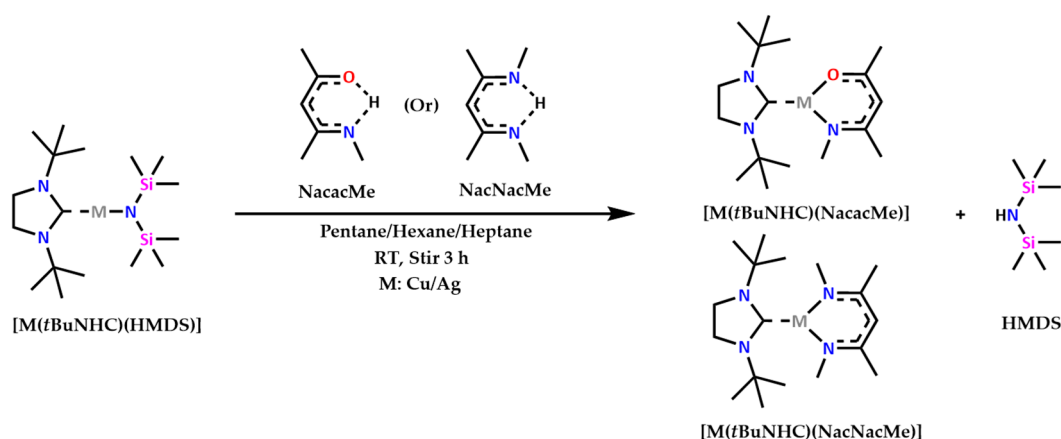
Scheme 1. A general synthesis scheme for *t*BuNHC-stabilized Cu^{I} and Ag^{I} complexes employed in this work.

3.2. ^{1}H-NMR Characterization

To gain the first insights into the purity and molecular integrity of the isolated complexes, ^{1}H-NMR spectra were obtained for all the complexes and compared with each other as depicted in Figure 2. Successful completion of the synthesis can be confirmed with the absence of the acidic proton beyond 10 ppm from the protonated ketoiminate or diketimine. As formulated, for all the four complexes only singlets were observed in their respective spectrum, and the purity of the isolated complexes was confirmed by the absence of residual proton signals. Signals A and C from protons of *t*BuNHC are the common peaks observed among the four complexes. The most intense peak A in all cases corresponds to the protons of tertiary butyl groups of the NHC owing to the higher number of protons (18) and thus affirms the successful bonding of the carbene to the metal centers. The singlet A is also found to be the most upfield at 1.3–1.5 ppm due to the strong shielding from the methyl groups of tertiary butyls. Interestingly, the protons of the tert-butyl groups are more deshielded for the copper complexes, presumably due to the lower electron density of copper compared to silver in close proximity to the tert-butyl groups. Further signals from the *t*BuNHC can be attributed to the singlet C between 2.7 and 2.8 ppm. Furthermore, singlet F can be attributed to the endocyclic proton of the anionic backbone of NacacMe and NacNacMe, owing to the partial electropositive nature resulting from electron delocalization and donation of electrons to the metal, especially when compared to the free and protonated ligand with more shielded contributions. Thus, in all the copper and silver analogs, singlet F shows the most downfield resonance at 4.6 ppm–5.0 ppm. A key observation includes the upfield shift of singlet F (<5 ppm) in NacNacMe relative to their NacacMe (>5 ppm) counterparts, which indicates the increased shielding because of higher overall delocalized electron density within the NacNacMe ligand.

A very interesting case is represented by the complex [Ag(*t*BuNHC) (NacacMe)]. A possible distinctive bonding situation can be observed due to the extra signals that are detected as neighbors to every peak for the NacacMe ligands. Conversely, no additional peaks are observed for the *t*BuNHC, suggesting that the NacacMe ligand might be bound to Ag in two different ways as depicted in Figure 2 (inset). With the given differences in the shifts of signal F and J, which correspond to the lone proton of the NacacMe ligand, it can be assumed that two structural isomers of [Ag(*t*BuNHC) (NacacMe)] are present. Signal J is significantly deshielded to 5.4 ppm and thus very comparable to the free and protonated NacacMe ligand. Thus, the ligand might be attached in a bidentate mode (N, O) in one case while, in the other case, the ligand is directly bound as a monodentate non-chelating ligand (over N or O). Under the given measurement conditions in NMR and in the solvent C$_6$D$_6$, an equilibrium of the two different isomers might be present. Considering the integral ratios, a mixture of 80% bidentate and 20% monodentate configurations can be assumed.
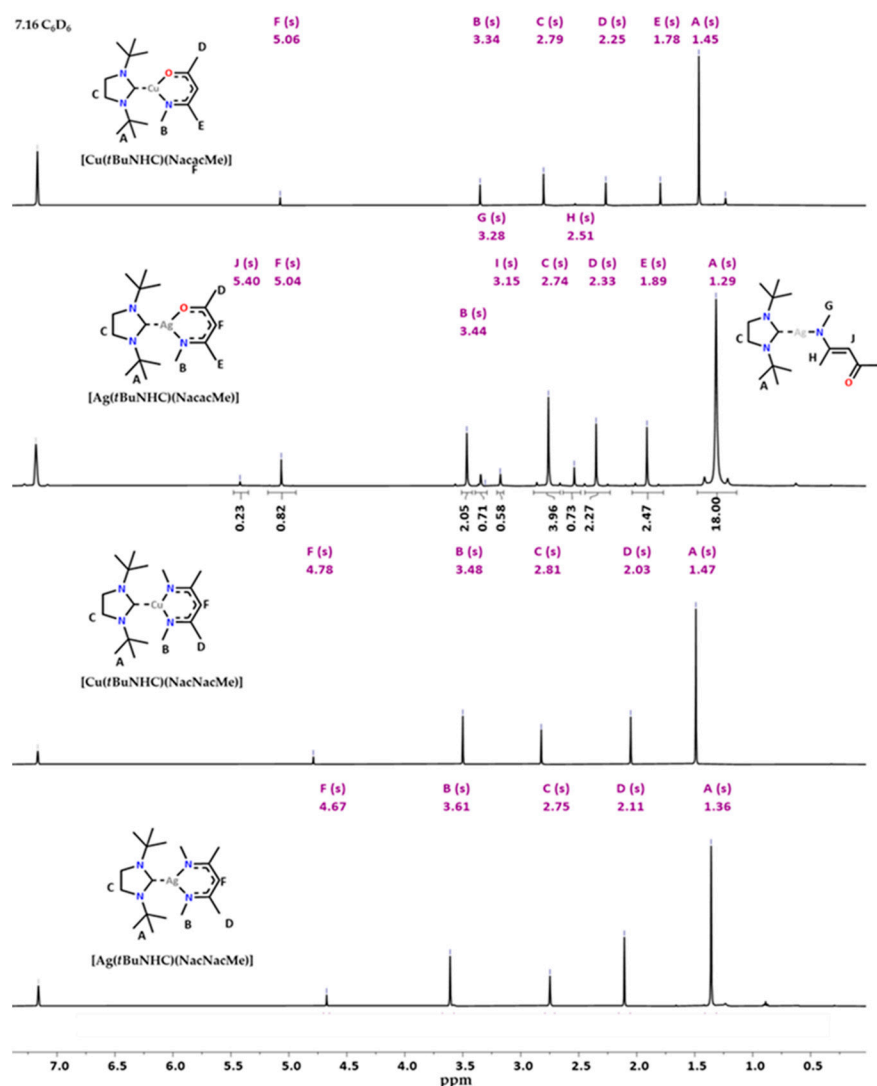
Figure 2. ^{1}H-NMR spectrum of all the four complexes stacked and referenced to C_6D_6 as the solvent. All the integrals are referenced to singlet A. Analyzed spectra of all the complexes are individually shown in Supplementary Materials.

However, for the [Ag(*t*BuNHC) (NacNacMe)] counterpart, such an anomaly is not observed in the respective ^{1}H-NMR spectrum. As expected, owing to their symmetrical structure, the signals from the protons of backbone methyl groups in NacNacMe are coupled as a singlet D (2.03 ppm and 2.11 ppm) while the methyl groups from amine are relatively deshielded, thus downshifted as singlet B at 3.48 ppm and 3.61 ppm for Cu and Ag variants, respectively. Furthermore, the binding of carbene to the metallic center can be confirmed in their respective ^{13}C-NMR spectra (Figures S2, S4, S6, and S9), where the signal is distinctively found in the region of above 200 ppm, owing to the heavy decrease in the electron density on the carbene. These values match with the literature for similar NHC Cu[I] and Ag[I] complexes [30,43]. A characteristic signal at greater than 180 ppm can be attributed to the carbonyl carbon peak for the NacacMe variants.

The precise structural insights gained from NMR are discussed in more detail below and are supported by SC-XRD and FT-IR spectroscopy.

3.3. Single Crystal XRD and FT-IR Analysis

SCXRD provides a precise structural situation and confirmation of the molecular integrity of the complexes in the solid state. Figure 3 portrays the solid-state structures of three complexes synthesized in this work along with those of [Cu(*t*BuNHC) (acac)]

and [Ag(*t*BuNHC) (acac)], previously reported by our group, for the sake of comparison and the trends seen in different structural parameters [35]. All the structures crystalize in monoclinic or orthorhombic crystal systems. The important bond lengths and bond angles are summarized in Table 2 below. The carbene-to-metal center bond length (C*–M) varies significantly with the Cu and Ag analogs. For [Cu(*t*BuNHC) (NacacMe)] and [Cu(*t*BuNHC) (NacNacMe)], the (C*–M) bond length shows a negligible difference (1.899 Å and 1.900 Å), whereas, in comparison to [Ag(*t*BuNHC) (NacacMe)], about 0.1 Å higher is observed, signifying that a higher ionic radius of Ag compared to Cu results in a longer bond length towards the ligands. This is further in accordance with the results acquired earlier in our group for similar Cu and Ag complexes [35]. Interestingly, the N1-Cu bond length is shorter than the O–Cu bond length in [Cu(*t*BuNHC) (NacacMe)]. This is possibly due to the increased electron density on the substituted amine; hence, there is stronger bonding with the Cu center than the oxygen.
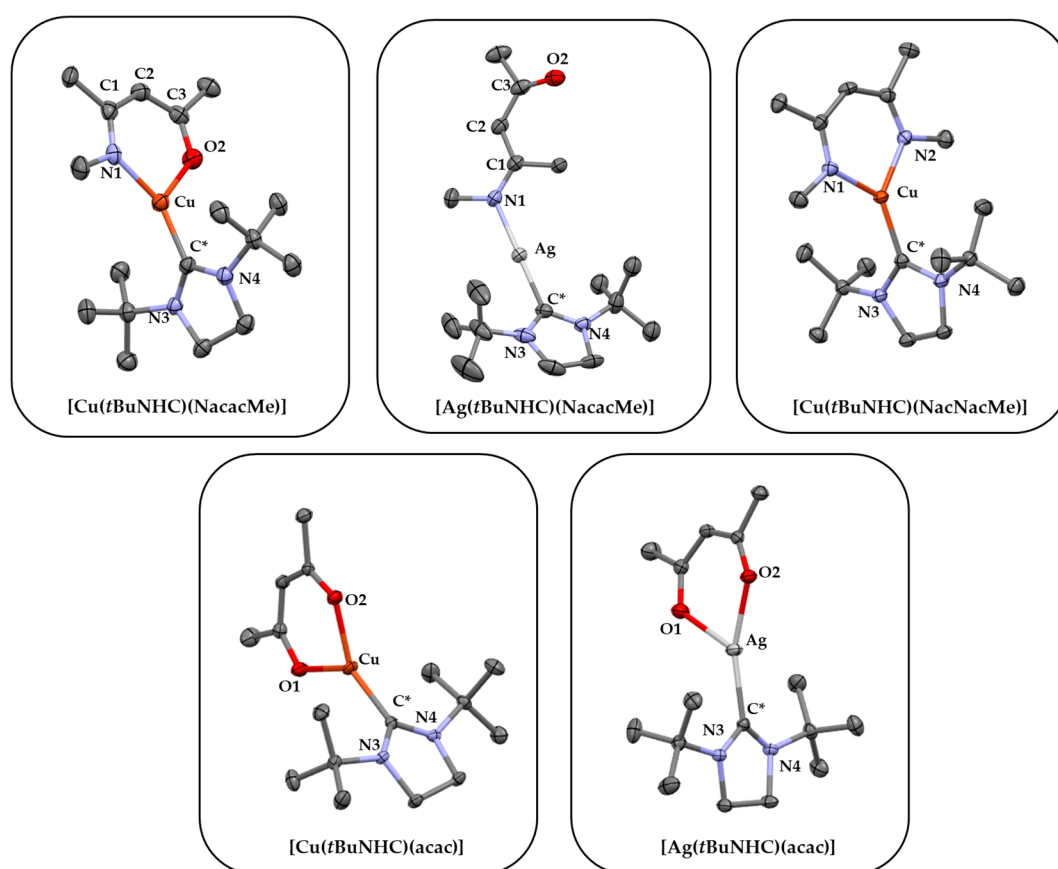
Figure 3. Solid-state structures obtained from the SC-XRD of three complexes synthesized in this work along with [Cu(tBuNHC) (acac)] and [Ag(tBuNHC) (acac)] solid-state structures published earlier by our group [35]. The ellipsoid probability is set at 50% and hydrogen atoms are omitted for clarity. The * in the figure represents the carbene carbon.

Table 2. Yields of the synthesized Cu[I] and Ag[I] complexes with their respective solvent system for crystallization.

Complex Name	Solvent System	Product Appearance	Yield (%)
[Cu(tBuNHC) (NacacMe)]	Hexane: THF (7:1)	Light yellow crystals	76
[Ag(tBuNHC) (NacacMe)]	Hexane: THF (7:2)	Colorless cubicle	66
[Cu(tBuNHC) (NacNacMe)]	Hexane: THF (7:2)	Colorless cubicle crystals	57
[Ag(tBuNHC) (NacNacMe)]	Hexane: THF (7:3)	Grey cubicle crystals	45

Furthermore, the shorter O–Cu bond length could be the result of electron delocalization within the NacacMe ligand. In the case of [Ag(*t*BuNHC) (NacacMe)], as discussed earlier, a different structure with a monodentate bonding motif is observed. In the solution phase, the complex exists in equilibrium with two structural isomers, whereas in the solid state, unusually, the complex prefers and crystalizes into the monodentate non-chelating isomer, as seen in Figure 3. In this case, the ligand is bound to the silver metal over the nitrogen, rather than over oxygen. The solid-state structure of [Ag(*t*BuNHC) (NacacMe)] further affirms that the NacacMe ligand is bonded as a mono-dentate ligand, which is only insufficiently explainable by ^{1}H-NMR as discussed before. Moreover, in comparison to [Ag(*t*BuNHC) (HMDS)], which has an Ag–N bond length of 2.079 Å, the Ag-N1 length of [Ag(*t*BuNHC) (NacacMe)] is 2.093 Å; thus, it is slightly longer than its predecessor starting complex, indicating the strong electron releasing group (ERG) nature of silyl groups and the non-chelating nature of NacacMe [33]. However, the Ag-N1 is significantly shorter in comparison to the homoleptic tetramer [(Ag(HMDS))₄], which has a bond length of 2.147 Å [46]. This can be explained by the heteroleptic design of the complex, delivering more room for the bonding of the anionic ligand. The C3-O2 bond length in [Ag(tBuNHC) (NacacMe)] is 1.250 Å, and conversely, the backbone carbon (C1-C2) and (C2-C3) are 1.409 Å and 1.419 Å, implying that the electrons are localized at the carbonyl group, thus confirming the non-chelating and non-delocalized nature of the anionic backbone.

From the crystal structure and crystallographic parameters of [Cu(*t*BuNHC) (NacNacMe)], it is clear that the NacNacMe attains a perfect resonance stabilization due to the exactly equal N1-Cu and N2-Cu bond lengths (1.966 Å), and thus has a better chelation effect on the metal center. The C*–Cu bond length is 1.900 Å, and, when it is compared to its previous generation [Cu(*t*BuNHC) (acac)] (1.888 Å), a slightly longer bond length is observed, suggesting that the NacNacMe ligand has a better and more pronounced stabilization on the Cu center than the acac ligand. This can be further observed with the different bond lengths (O1-Cu and O2-Cu) of acac, implying a weaker resonance stabilization compared to the NacNacMe variant. The NacNacMe ligand is also observed to be in the same plane, owing to the strong resonance stabilization within the anionic backbone. The important bond lengths and angles are summarized in Table 3, below. Despite the successful isolation of crystals for [Ag(*t*BuNHC) (NacNacMe)], the determination of the crystal structure and molecular parameters was not conveniently achieved. Initial attempts to solve the structure at least indicate a similar bidentate binding mode as seen for [Cu(*t*BuNHC) (NacNacMe)]; however, the structure could not be refined to acceptable R-values that would be reasonable for publication.

Table 3. Important bond angles and bond lengths from the crystal structures obtained.

Parameters	[Cu(*t*BuNHC) (NacacMe)]	[Ag(*t*BuNHC) (NacacMe)]	[Cu(*t*BuNHC) (NacNacMe)]	[Cu(*t*BuNHC) (acac)]	[Ag(*t*BuNHC) (acac)]
C*–M	1.899 Å	2.096 Å	1.900 Å	1.888 Å	2.091 Å
(O1/N1)-M	1.943 Å	2.093 Å	1.966 Å	2.051 Å	2.341 Å
(O2/N2)-M	2.031 Å	-	1.966 Å	1.969 Å	2.180 Å
(N1/O1)-M-(N2/O2)	94.76°	-	97.25°	92.09°	82.44°
N3-C*-N4	108.38°	109.33°	107.4°	108.10°	108.92°
Structure	Monoclinic	Monoclinic	Orthorhombic	Monoclinic	Monoclinic

Further elucidation of the functional groups and bonding situation present in different complexes in the solid state are analyzed via FTIR spectroscopy as shown in Figure 4.

Firstly, the absence of an NH-stretching frequency beyond 3000 cm^{-1} affirms the successful ligand exchange, in all four complexes without residual protonated N–H species. This once again confirms the purity of the synthesized and isolated complexes. Secondly, the C–H stretches below 3000 cm^{-1} are observed at 2900 cm^{-1} among all the complexes owning to the presence of methyl groups in the NacacMe/NacNacMe ligand and in the tertiary butyl group of NHC. Furthermore, the characteristic high-intensity band for C–H bending is also seen in the 1300 cm^{-1} region. C–N and C–O stretches are present in the region of 1200 cm^{-1}, in between the C=O stretching (1700 cm^{-1}) and C–O (1000 cm^{-1})

stretching as a result of partial resonance of the pi-bond. The C=C bond stretches from the anionic ligand likely correspond to the 1500 cm^{-1} region, and the C=O stretches are likely overlapped by other peaks in the same region due to the delocalization of electrons in the NacNacMe/NacacMe ligands. The common low-intensity peak in the 500 cm^{-1} regions among all the complexes should possibly correspond to the carbene-metal frequency (C*–M) [47,48].
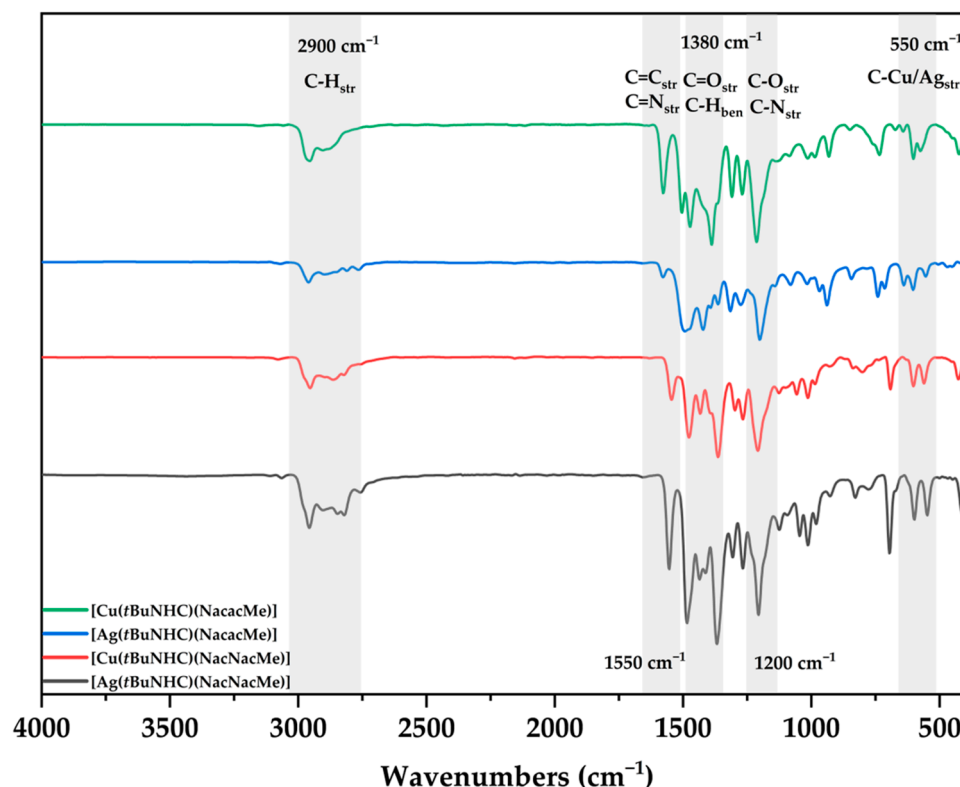

Figure 4. FTIR spectra of all the four Cu and Ag complexes stacked from top to bottom. Key stretching and bending frequency ranges are marked.

In comparison with each other, particularly in the fingerprint region (<1500 cm^{-1}), the NacNacMe complexes, [Cu(*t*BuNHC) (NacNacMe)], and [Ag(*t*BuNHC) (NacNacMe)] almost have identical spectra and bands. This further substantiates the similar structural situation in both complexes. Conversely, this norm is not observed for the NacacMe variants, [Cu(*t*BuNHC) (NacacMe)], and [Ag(*t*BuNHC) (NacacMe)]. Pronounced differences in the spectrum of [Ag(*t*BuNHC) (NacacMe)] around the 1500 cm^{-1} region are visible; however, such drastic differences in the peaks for [Cu(*t*BuNHC) (NacacMe)] with NacNacMe variants are not observed. This, indeed, once more confirms the distinctive bonding of the NacacMe ligand in [Ag(*t*BuNHC) (NacacMe)]. Furthermore, the nature of the synthesized complexes is confirmed via mass spectrometry (Figures S11–S13), specifically using LIFDI-MS (liquid injection field desorption ionization mass spectrometry), for which we previously reported its advantage in using highly unstable and reactive organometallic complexes [49].

3.4. Thermal Analysis

To evaluate the suitability of the synthesized complex as potential precursors in vapor phase deposition processes such as CVD and ALD, the thermal properties of the complexes are of the utmost importance. The evaluation of thermal properties such as volatility and thermal stability are required for identifying potential evaporation temperatures in CVD and ALD, while also delivering information about suitable deposition temperature windows. Thus, with the help of TGA and DSC, we are able to derive these valuable parameters, such as the onset temperature of evaporation, melting, and decomposition

points, as well as a residual fraction after heating to the desired temperature in the experiment. Figure 5 depicts the TGA/DSC curves of the synthesized complexes from RT to 500 °C. At first glance, as seen in Figure 5, a considerable amount of residual mass is present for both the Cu and Ag complexes. In general, the silver complexes were found to be thermally less stable than their copper analogs, which is in line with our previous studies for closely related Cu and Ag complexes [35]. Stronger and thus shorter bonds in the case of Cu might enhance the thermal stabilities compared to the related Ag complexes. For [Cu(*t*BuNHC) (NacacMe)], the onset temperature of evaporation (1% mass loss) is located at 115 °C, while the active volatilization of the complex starts at 173 °C in a single-step thermal profile. The TG curve settles down at a constant residual mass of 16% after heating to 550 °C, which theoretically matches the Cu mass percentage (18%) in [Cu(*t*BuNHC) (NacacMe)], assuming it decomposes cleanly. However, the DSC profile does not indicate any clear and characteristic exothermic peaks that could be attributed to decomposition events, other than the endothermic peak at 99 °C, which can probably be attributed to the melting point of the complex. Most probably, both evaporation of the complex and partial decomposition are occurring in parallel. For its direct Ag analog [Ag(*t*BuNHC) (NacacMe)], a two-step evaporation behavior is observed, implying the existence of a decomposition event starting at 140 °C, which is supported by a clearly visible exothermic peak from its DSC profile. Nevertheless, the onset of evaporation starts at a temperature of 89 °C. After the first decomposition event, the curve enters a second step where the decomposition products are subsequently volatilized, leading to a constant plateau with a residual mass of 35% after heating to 240 °C.
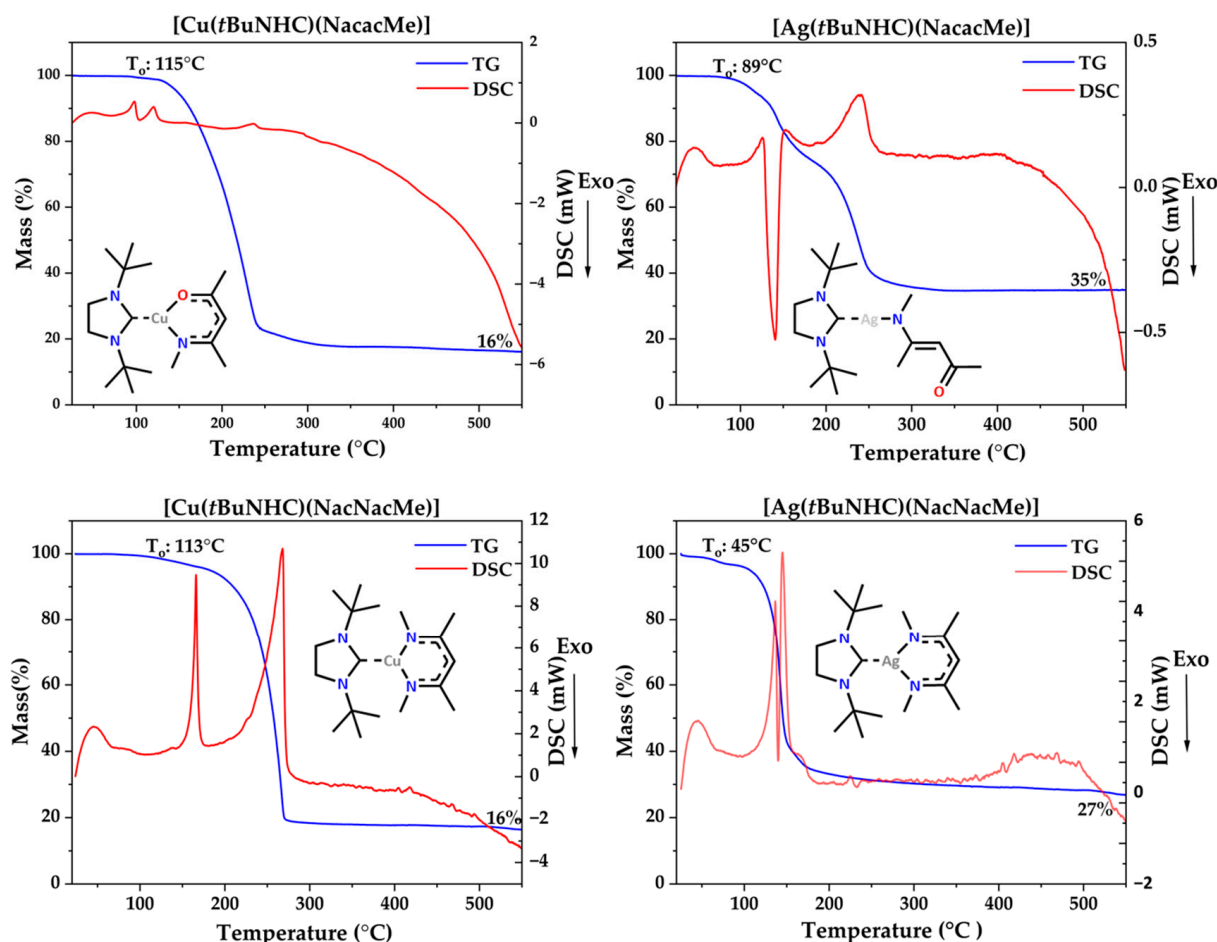
Figure 5. TGA and DSC of the four Cu and Ag complexes with their structure (inset). T_O: Temperature of onset of mass loss.

For the nitrogen-only coordinated NacNacMe complexes, a similar thermal trend to its NacacMe counterparts is also observed. The [Cu(*t*BuNHC) (NacNacMe)] complex has an onset of evaporation at 113 °C, which is only slightly more volatile than [Cu(*t*BuNHC) (NacacMe)] and follows with a one-step volatilization profile. A clear endothermic peak at 165 °C from its DSC curve might indicate the melting point of the complex and an active volatilization is observed at 240 °C accompanied by a characteristic endothermic peak from DSC. Nonetheless, the curve settles down at a constant residual mass of 16% which is the same as observed for [Cu(*t*BuNHC) (NacNacMe)]. The complex was further tested if it was sublimable under reduced pressure, and the complex sublimed at 110 °C and 1 mbar pressure with minimal residue left behind (Figure S7 (inset)). This implies that the complex could be successfully evaporated under reduced pressure and a reasonable temperature, which indicates a potential use as a precursor in vapor deposition processes. The parent Ag variant, [Ag(*t*BuNHC) (NacNacMe)], interestingly exhibits the most volatile nature with an onset temperature of evaporation at 45 °C and active volatilization at 132 °C, coupled with a strong endothermic event interrupted by a strong exothermic event, indicating the onset of decomposition at 139 °C. Although the TG curve shows a single-step evaporation profile, the prominent decomposition event likely leads to a high residual mass of 27%, matching the theoretical mass percentage of Ag (28%) in [Ag(*t*BuNHC) (NacNacMe)], if full decomposition to metallic Ag is assumed.

Table 4 shows a comprehensive overview of all the important parameters from their respective TGA/DSC curves (Figure 5). Overall, [Ag(*t*BuNHC) (NacNacMe)] showed the most volatile nature among the four complexes, followed by the NacacMe variant, [Ag(*t*BuNHC) (NacacMe)]. In a similar fashion, [Cu(*t*BuNHC) (NacNacMe)] was found to be only slightly more volatile than the [Cu(*t*BuNHC) (NacacMe)] again, indicating an increase in volatility going from the NacacMe to NacNacMe ligand. However, in all cases, a considerable amount of residual mass is observed. Other than the [Ag(*t*BuNHC) (NacacMe)] complex, the remaining complexes show a mass percentage equivalent to their theoretical metallic mass percentage. The crystalline nature of the residue fits the XRD pattern of crystalline copper and silver (Figures S16 and S17) for the [Cu(*t*BuNHC) (NacNacMe)] and [Ag(*t*BuNHC) (NacacMe)], respectively. This indicates and affirms that the theoretical residual masses are in agreement with metallic copper and silver. However, for [Ag(*t*BuNHC) (NacacMe)], additional reflections in the XRD pattern are observed. This is possibly from the crystalline impurity corresponding to its first decomposition event.

Table 4. Important temperature points of the synthesized complexes from TG/DSC.

Complex Name	1% Mass Loss (°C)	Melting Point (°C)	Decomposition (°C)	Residual Mass (%)	1 Torr Temperature (°C)
[Cu(*t*BuNHC) (NacacMe)]	115	99	-	16	185.02
[Ag(*t*BuNHC) (NacacMe)]	89	-	140	35	-
[Cu(*t*BuNHC) (NacNacMe)]	113	165	-	16	186
[Ag(*t*BuNHC) (NacNacMe)]	45	136	139	27	-

The vapor pressure plots give valuable information on the precursor vaporization temperature. Figures S14 and S15 depict the vapor vs. temperature plot for the Cu variants [50]. However, this method fails if the TGA produces a multi-step curve or observable decomposition (Figure 5). Thus, the 1 Torr vapor pressure temperature could not be calculated for the Ag analogs. In summary, these complexes can be potentially exploited in MOCVD, where intact evaporation of the precursor and decomposition at higher temperatures is a necessity. Especially in low-temperature MOCVD, the Ag precursor [Ag(*t*BuNHC) (NacNacMe)] might be used as it features a low onset temperature of evaporation and low decomposition temperatures with a suitable process window between evaporation and decomposition. Potential processes might only be limited to very low substrate temperatures. On the other hand, the copper complex, [Cu(*t*BuNHC) (NacNacMe)], can potentially be used as an ALD and CVD precursor in a broader temperature regime, given its higher thermal

stability to substantiate this claim; a computational approach via density functional theory (DFT) might further confirm the thermal decomposition pathways of the aforementioned complexes. Although the precursors known in the literature feature decent volatility and thermal stability, heteroatoms such as Si, F, P, or O are present in the ligand sphere of the precursors. This is necessary for the stabilization of such complexes; however, these heteroatoms might result in thin film contaminants during CVD or ALD. Additionally, the reactivity of these known Cu(I) or Ag(I) precursors is limited. Moreover, because of the absence of such heteroatoms and a higher reactivity, our new precursors are already an attractive option and a step towards better precursors in comparison to the prominent Cu^I and Ag^I precursors (Table S1). With the most promising precursor from this row, the highly reactive [Cu(*t*BuNHC) (NacNacMe)], MOCVD, and ALD deposition experiments should be carried out in the future to further confirm their suitability.

4. Conclusions

New Cu^I and Ag^I complexes stabilized by NHCs with anionic ketoiminate (NacacMe) and diketiminate (NacNacMe) ligands were successfully synthesized, characterized, and evaluated for their potential use in MOCVD and ALD. The ketoiminate and diketiminate ligands were chosen to systematically enhance the reactivity of the precursors and reduce the number of heteroatoms in the ligand sphere that might lead to thin-film contamination. Two structural isomers were observed for the diketminiate-based complex [Ag(*t*BuNHC) (NacacMe)] and found to coexist in the solvated state, whereas in the solid state the monodentate non-chelating isomer is preferred. Interestingly, all the other complexes exhibit bidentate bonding to the metal ion. The potential use of these complexes as precursors for MOCVD and ALD was evaluated using TGA/DSC, in which an increase in volatility was observed upon changing the anionic ligand from NacacMe to NacNacMe. In general, the Ag analogs in comparison to Cu were found to be more volatile but thermally more unstable. However, all four complexes exhibit residual mass, likely from thermal decomposition during evaporation, and thus are suitable candidates for precursors for the MOCVD of metallic Cu and Ag films. Only the Cu complex [Cu(*t*BuNHC) (NacacMe] could be successfully sublimed and exhibited the highest temperature stability, which is very interesting as a precursor in ALD. The suitability of the precursors in actual deposition experiments via MOCVD and ALD will be the focus of our future studies.

References

1. Matula, R.A. Electrical Resistivity of Copper, Gold, Palladium, and Silver. *J. Phys. Chem. Ref. Data* **1979**, *8*, 1147–1298. [CrossRef]
2. Nath, P.; Chopra, K.L. Thermal Conductivity of Copper Films. *Thin Solid Film.* **1974**, *20*, 53–62. [CrossRef]
3. Ho, C.Y.; Ackerman, M.W.; Wu, K.Y.; Oh, S.G.; Havill, T.N. Thermal Conductivity of Ten Selected Binary Alloy Systems. *J. Phys. Chem. Ref. Data* **1978**, *7*, 959–1178. [CrossRef]
4. Stoppa, M.; Chiolerio, A. Wearable Electronics and Smart Textiles: A Critical Review. *Sensors* **2014**, *14*, 11957–11992. [CrossRef]
5. Zhao, J.; Zheng, X.; Deng, Y.; Li, T.; Shao, Y.; Gruverman, A.; Shield, J.; Huang, J. Is Cu a Stable Electrode Material in Hybrid Perovskite Solar Cells for a 30-Year Lifetime? *Energy Environ. Sci.* **2016**, *9*, 3650–3656. [CrossRef]
6. Bellchambers, P.; Walker, M.; Huband, S.; Dirvanauskas, A.; Hatton, R.A. Enhanced Oxidation Stability of Transparent Copper Films Using a Hybrid Organic-Inorganic Nucleation Layer. *ChemNanoMat* **2019**, *5*, 619–624. [CrossRef]
7. Li, B.; Sullivan, T.D.; Lee, T.C.; Badami, D. Reliability Challenges for Copper Interconnects. *Microelectron. Reliab.* **2004**, *44*, 365–380. [CrossRef]
8. Andricacos, P.C.; Uzoh, C.; Dukovic, J.O.; Horkans, J.; Deligianni, H. Damascene Copper Electroplating for Chip Interconnections. *IBM J. Res. Dev.* **1998**, *42*, 567–574. [CrossRef]
9. Buchanan, K. The Evolution of Interconnect Technology for Silicon Integrated Circuitry. In Proceedings of the GaAs Mantech Conference, San Diego, CA, USA, 19 April 2002. Available online: https://citeseerx.ist.psu.edu/document?repid=rep1&type=pdf&doi=1098682b0717c1267a22eb343405ee87b21f26f1 (accessed on 15 September 2023).
10. Zilberberg, K.; Riedl, T. Metal-Nanostructures—A Modern and Powerful Platform to Create Transparent Electrodes for Thin-Film Photovoltaics. *J. Mater. Chem. A* **2016**, *4*, 14481–14508. [CrossRef]
11. Hu, T.; Becker, T.; Pourdavoud, N.; Zhao, J.; Brinkmann, K.O.; Heiderhoff, R.; Gahlmann, T.; Huang, Z.; Olthof, S.; Meerholz, K.; et al. Indium-Free Perovskite Solar Cells Enabled by Impermeable Tin-Oxide Electron Extraction Layers. *Adv. Mater.* **2017**, *29*, 1606656. [CrossRef]
12. Wang, D.; Zhang, Y.; Lu, X.; Ma, Z.; Xie, C.; Zheng, Z. Chemical Formation of Soft Metal Electrodes for Flexible and Wearable Electronics. *Chem. Soc. Rev.* **2018**, *47*, 4611–4641. [CrossRef] [PubMed]
13. Park, J.H.; Ambwani, P.; Manno, M.; Lindquist, N.C.; Nagpal, P.; Oh, S.-H.; Leighton, C.; Norris, D.J. Single-Crystalline Silver Films for Plasmonics. *Adv. Mater.* **2012**, *24*, 3988–3992. [CrossRef] [PubMed]
14. Santbergen, R.; Temple, T.L.; Liang, R.; Smets, A.H.M.; van Swaaij, R.A.C.M.M.; Zeman, M. Application of Plasmonic Silver Island Films in Thin-Film Silicon Solar Cells. *J. Opt.* **2012**, *14*, 024010. [CrossRef]
15. Mansuripur, M.; Zakharian, A.R.; Lesuffleur, A.; Oh, S.-H.; Jones, R.J.; Lindquist, N.C.; Im, H.; Kobyakov, A.; Moloney, J.V. Plasmonic Nano-Structures for Optical Data Storage. *Opt. Express* **2009**, *17*, 14001–14014. [CrossRef]
16. Lee, K.J.; Wei, R.; Wang, Y.; Zhang, J.; Kong, W.; Chamoli, S.K.; Huang, T.; Yu, W.; ElKabbash, M.; Guo, C. Gigantic Suppression of Recombination Rate in 3D Lead-Halide Perovskites for Enhanced Photodetector Performance. *Nat. Photonics* **2023**, *17*, 236–243. [CrossRef]
17. Barnes, W.L.; Dereux, A.; Ebbesen, T.W. Surface Plasmon Subwavelength Optics. *Nature* **2003**, *424*, 824–830. [CrossRef] [PubMed]
18. Baburin, A.S.; Merzlikin, A.M.; Baryshev, A.V.; Ryzhikov, I.A.; Panfilov, Y.V.; Rodionov, I.A. Silver-Based Plasmonics: Golden Material Platform and Application Challenges [Invited]. *Opt. Mater. Express* **2019**, *9*, 611–642. [CrossRef]
19. George, S.M. Atomic Layer Deposition: An Overview. *Chem. Rev.* **2010**, *110*, 111–131. [CrossRef]
20. Pierson, H.O. 15—CVD in Optoelectronic and Ferroelectric Applications. In *Handbook of Chemical Vapor Deposition (CVD)*, 2nd ed.; Pierson, H.O., Ed.; William Andrew Publishing: Norwich, NY, USA, 1999; pp. 384–402. ISBN 978-0-8155-1432-9.
21. Baptista, A.; Silva, F.; Porteiro, J.; Míguez, J.; Pinto, G. Sputtering Physical Vapour Deposition (PVD) Coatings: A Critical Review on Process Improvement and Market Trend Demands. *Coatings* **2018**, *8*, 402. [CrossRef]
22. Schalk, N.; Tkadletz, M.; Mitterer, C. Hard Coatings for Cutting Applications: Physical vs. Chemical Vapor Deposition and Future Challenges for the Coatings Community. *Surf. Coat. Technol.* **2022**, *429*, 127949. [CrossRef]
23. Leskelä, M.; Ritala, M. Atomic Layer Deposition (ALD): From Precursors to Thin Film Structures. *Thin Solid Film.* **2002**, *409*, 138–146. [CrossRef]
24. Dias, H.V.R. Polyfluorinated ligand-supported organometallic complexes of copper, silver, and gold. *Pure Appl. Chem.* **2010**, *82*, 649–656. [CrossRef]
25. Hagen, D.J.; Pemble, M.E.; Karppinen, M. Atomic Layer Deposition of Metals: Precursors and Film Growth. *Appl. Phys. Rev.* **2019**, *6*, 041309. [CrossRef]
26. Cohen, S.L.; Liehr, M.; Kasi, S. Mechanisms of Copper Chemical Vapor Deposition. *Appl. Phys. Lett.* **1992**, *60*, 50–52. [CrossRef]

27. Li, Z.; Rahtu, A.; Gordon, R.G. Atomic Layer Deposition of Ultrathin Copper Metal Films from a Liquid Copper(I) Amidinate Precursor. *J. Electrochem. Soc.* **2006**, *153*, C787. [CrossRef]

28. Li, Z.; Barry, S.T.; Gordon, R.G. Synthesis and Characterization of Copper(I) Amidinates as Precursors for Atomic Layer Deposition (ALD) of Copper Metal. *Inorg. Chem.* **2005**, *44*, 1728–1735. [CrossRef] [PubMed]

29. Coyle, J.P.; Dey, G.; Sirianni, E.R.; Kemell, M.L.; Yap, G.P.A.; Ritala, M.; Leskelä, M.; Elliott, S.D.; Barry, S.T. Deposition of Copper by Plasma-Enhanced Atomic Layer Deposition Using a Novel N-Heterocyclic Carbene Precursor. *Chem. Mater.* **2013**, *25*, 1132–1138. [CrossRef]

30. Boysen, N.; Misimi, B.; Muriqi, A.; Wree, J.-L.; Hasselmann, T.; Rogalla, D.; Haeger, T.; Theirich, D.; Nolan, M.; Riedl, T.; et al. A Carbene Stabilized Precursor for the Spatial Atomic Layer Deposition of Copper Thin Films. *Chem. Commun.* **2020**, *56*, 13752–13755. [CrossRef]

31. Szłyk, E.; Piszczek, P.; Grodzicki, A.; Chaberski, M.; Goliński, A.; Szatkowski, J.; Błaszczyk, T. CVD of AgI Complexes with Tertiary Phosphines and Perfluorinated Carboxylates—A New Class of Silver Precursors. *Chem. Vap. Depos.* **2001**, *7*, 111–116. [CrossRef]

32. Shapiro, M.J.; Lackey, W.J.; Hanigofsky, J.A.; Hill, D.N.; Carter, W.B.; Barefield, E.K. Chemical Vapor Deposition of Silver Films for Superconducting Wire Applications. *J. Alloys Compd.* **1992**, *187*, 331–349. [CrossRef]

33. Boysen, N.; Hasselmann, T.; Karle, S.; Rogalla, D.; Theirich, D.; Winter, M.; Riedl, T.; Devi, A. An N-Heterocyclic Carbene Based Silver Precursor for Plasma-Enhanced Spatial Atomic Layer Deposition of Silver Thin Films at Atmospheric Pressure. *Angew. Chem. Int. Ed.* **2018**, *57*, 16224–16227. [CrossRef] [PubMed]

34. Hasselmann, T.; Misimi, B.; Boysen, N.; Zanders, D.; Wree, J.-L.; Rogalla, D.; Haeger, T.; Zimmermann, F.; Brinkmann, K.O.; Schädler, S.; et al. Silver Thin-Film Electrodes Grown by Low-Temperature Plasma-Enhanced Spatial Atomic Layer Deposition at Atmospheric Pressure. *Adv. Mater. Technol.* **2023**, *8*, 2200796. [CrossRef]

35. Boysen, N.; Philip, A.; Rogalla, D.; Karppinen, M.; Devi, A. Role of Anionic Backbone in NHC-Stabilized Coinage Metal Complexes: New Precursors for Atomic Layer Deposition. *Chem. Eur. J.* **2022**, *28*, e202103798. [CrossRef] [PubMed]

36. Devi, A. 'Old Chemistries' for New Applications: Perspectives for Development of Precursors for MOCVD and ALD Applications. *Coord. Chem. Rev.* **2013**, *257*, 3332–3384. [CrossRef]

37. Huster, N.; Ghiyasi, R.; Zanders, D.; Rogalla, D.; Karppinen, M.; Devi, A. SnO Deposition via Water Based ALD Employing Tin(II) Formamidinate: Precursor Characterization and Process Development. *Dalton Trans.* **2022**, *51*, 14970–14979. [CrossRef]

38. Zanders, D.; Obenlüneschloß, J.; Wree, J.-L.; Jagosz, J.; Kaur, P.; Boysen, N.; Rogalla, D.; Kostka, A.; Bock, C.; Öhl, D.; et al. Unveiling Ruthenium(II) Diazadienyls for Gas Phase Deposition Processes: Low Resistivity Ru Thin Films and Their Performance in the Acidic Oxygen Evolution Reaction. *Adv. Mater. Interfaces* **2022**, *9*, 2201709. [CrossRef]

39. Baraldi, P.G.; Simoni, D.; Manfredini, S. An Improved Preparation of Enaminones from 1,3-Diketones and Ammonium Acetate or Amine Acetates. *Synthesis* **1983**, *1983*, 902–903. [CrossRef]

40. Taftaf, M.; Zuideveld, M.A.; Batinas-Geurts, A.A.; Sainani, J.B.; Vimalkumar, M.P.; Zakharov, V.A.; Bukatov, G.D.; Sergeev, S.A.; Ghalit, N. Catalyst Composition for Polymerization of Olefins. U.S. Patent 10059656B2, 19 December 2014.

41. Stalzer, M.M.; Lohr, T.L.; Marks, T.J. Synthesis, Characterization, and Thermal Properties of *N*-alkyl β-Diketiminate Manganese Complexes. *Inorg. Chem.* **2018**, *57*, 3017–3024. [CrossRef] [PubMed]

42. McGeachin, S.G. Synthesis and Properties of Some β-Diketimines Derived from Acetylacetone, and Their Metal Complexes. *Can. J. Chem.* **1968**, *46*, 1903–1912. [CrossRef]

43. Coyle, J.P.; Sirianni, E.R.; Korobkov, I.; Yap, G.P.A.; Dey, G.; Barry, S.T. Study of Monomeric Copper Complexes Supported by N-Heterocyclic and Acyclic Diamino Carbenes. *Organometallics* **2017**, *36*, 2800–2810. [CrossRef]

44. Dilworth, J.R.; Hussain, W.; Hutson, A.J.; Jones, C.J.; Mcquillan, F.S.; Mayer, J.M.; Arterburn, J.B. Tetrahalo Oxorhenate Anions. In *Inorganic Syntheses*; John Wiley & Sons, Ltd.: Hoboken, NJ, USA, 1996; pp. 257–262. ISBN 978-0-470-13262-3.

45. Weber, M.; Boysen, N.; Graniel, O.; Sekkat, A.; Dussarrat, C.; Wiff, P.; Devi, A.; Muñoz-Rojas, D. Assessing the Environmental Impact of Atomic Layer Deposition (ALD) Processes and Pathways to Lower It. *ACS Mater. Au* **2023**, *3*, 274–298. [CrossRef]

46. Hitchcock, P.B.; Lappert, M.F.; Pierssens, L.J.-M. Synthesis and X-ray Molecular Structures of the Silver(I) Amides [{Ag[μ-N(SiMe₃)₂]}₄] and [{Ag[μ-NCMe₂(CH₂)₃CMe₂]}₄]. *Chem. Commun.* **1996**, *10*, 1189–1190. [CrossRef]

47. Teyssot, M.-L.; Nauton, L.; Canet, J.-L.; Cisnetti, F.; Chevry, A.; Gautier, A. Aromatic Nitrogen Donors for Efficient Copper(I)–NHC CuAAC under Reductant-Free Conditions. *Eur. J. Org. Chem.* **2010**, *2010*, 3507–03515. [CrossRef]

48. Pellei, M.; Gandin, V.; Marzano, C.; Marinelli, M.; Del Bello, F.; Santini, C. The First Water-Soluble Copper(I) Complexes Bearing Sulfonated Imidazole- and Benzimidazole-Derived N-Heterocyclic Carbenes: Synthesis and Anticancer Studies. *Appl. Organomet. Chem.* **2018**, *32*, e4185. [CrossRef]

49. Boysen, N.; Devi, A. Liquid Injection Field Desorption/Ionization as a Powerful Tool to Characterize Volatile, Labile, and Reactive Metal–Organic Complexes. *Eur. J. Mass Spectrom.* **2023**, *29*, 12–20. [CrossRef]

50. Price, D. Vapor Pressure Determination by Thermogravimetry. *Thermochim. Acta* **2001**, *367*, 253–262. [CrossRef]

51. Smura, C.F.; Parker, D.R.; Zbiri, M.; Johnson, M.R.; Gál, Z.A.; Clarke, S.J. High-Spin Cobalt(II) Ions in Square Planar Coordination: Structures and Magnetism of the Oxysulfides Sr₂CoO₂Cu₂S₂ and Ba₂CoO₂Cu₂S₂ and Their Solid Solution. *J. Am. Chem. Soc.* **2011**, *133*, 2691–2705. [CrossRef]

52. Owen, E.A.; Williams, G.I. A Low-Temperature X-Ray Camera. *J. Sci. Instrum.* **1954**, *31*, 49. [CrossRef]

53. Moon, D.-Y.; Kim, W.-S.; Kim, T.-S.; Kang, B.-W.; Park, J.-W.; Yeom, S.J.; Kim, J.H. Atomic Layer Deposition of Copper Seed Layers from a (Hfac)Cu(VTMOS) Precursor. *JKPS* **2009**, *54*, 1330–1333. [CrossRef]

54. Minjauw, M.M.; Solano, E.; Sree, S.P.; Asapu, R.; Van Daele, M.; Ramachandran, R.K.; Heremans, G.; Verbruggen, S.W.; Lenaerts, S.; Martens, J.A.; et al. Plasma-Enhanced Atomic Layer Deposition of Silver Using Ag(Fod) (PEt3) and NH3-Plasma. *Chem. Mater.* **2017**, *29*, 7114–7121. [CrossRef]